PAPER

Selective catalytic reduction of NO over W–Zr-O$_x$/TiO$_2$: performance study of hierarchical pore structure†

Qijie Jin,*[a] Yao Lu,[a] Wenyu Ji,[a] Bo Yang,[b] Mutao Xu,[a] Zhiwei Xue,[c] Yi Dai[a] and Haitao Xu [ID] *[a]

A series of W–Zr-O$_x$/TiO$_2$ catalysts with hierarchical pore structure were prepared and used for selective catalytic reduction of NO by NH$_3$. Results showed that the 5C-WZ/T had a hierarchical pore structure, and exhibited high catalytic activity and good resistance to water and sulfur poisoning. The activity of the 5C-WZ/T catalyst was close to 100% in the range of 350–500 °C. The hierarchical pore structure not only improved the specific surface area, redox performance, and acid quantity, but also enabled the catalyst to expose more active sites and improved the catalytic performance. Although the reducing atmosphere caused by citric acid monohydrate reduced the chemical adsorption oxygen concentration, it increased the oxygen mobility and Ti^{3+} ion concentration, which was more conducive to the improvement of catalytic activity. Finally, the NH$_3$-SCR reaction over 5C-WZ/T catalyst followed L–H and E–R mechanisms. The monodentate nitrite, bidentate nitrate, gas-phase NO$_2$, coordinated NH$_3$ and NH$_4^+$ were the main reaction intermediates.

1. Introduction

Nitrogen oxides (NO$_x$) are one of the main causes for deteriorating the atmosphere, causing secondary pollution such as haze and acid rain.[1–3] Following the achievement of ultra-low NO$_x$ emissions in the thermal power industry, the treatment of diesel engine exhaust is an important measure to reduce NO$_x$ emissions. Selective catalytic reduction (SCR) has also become the mainstream technology for treating NO$_x$ due to its excellent catalytic performance.[4] According to the temperature of the flue gas, the catalyst is mainly divided into three types: low temperature, medium temperature and high temperature.[5–7] The flue gas temperature is usually higher than 450 °C (high temperature region) when the diesel engine is running at full speed. For commercial high-temperature catalysts, the common ones are mainly V$_2$O$_5$(WO$_3$)/TiO$_2$ and molecular sieves.[8–10] However, V$_2$O$_5$(WO$_3$)/TiO$_2$ is gradually being replaced due to its toxicity.[11–13] Molecular sieve catalysts have poor hydrothermal stability at high temperatures, resulting in their

structure being destroyed under long-term high temperature and high humidity conditions, which affects catalytic performance.[14–16] Therefore, the development of SCR catalysts with stable catalytic performance under high temperature and high humidity conditions has become an important need.

Acidity is the main factor affecting the catalytic activity for the NH$_3$-SCR at high temperature.[17–19] WO$_3$ not only has rich Lewis acid, but also can form solid super acid with ZrO$_2$.[20–22] In our previous work, it proved that W–Zr-O$_x$/TiO$_2$ can be applied to SCR at high temperature.[23] However, TiO$_2$ was used directly as the carrier in the previous study. WO$_3$ and ZrO$_2$ were not uniformly dispersed on the surface of the carrier, and the pores of the catalyst were not rich enough. On the other hand, TiOSO$_4$ is soluble in water and forms a uniform mixed solution with ammonium metatungstate and zirconium oxychloride. Therefore, in theory, these three precursors can prepare a uniformly dispersed catalyst. In addition, citric acid monohydrate can not only be used as a complexing agent to inhibit the reaction of ammonium metatungstate and zirconium oxychloride, but also can be used as a pore-forming agent during the roasting process.

In order to verify the rationality of the above speculation, a series of W–Zr-O$_x$/TiO$_2$ catalysts with hierarchical pore structure were prepared for NH$_3$-SCR. The effects of hierarchical pore structure, chemisorbed oxygen concentration and specific surface area on the NH$_3$-SCR were explored.

2. Experimental

The details about characterization were provided in ESI.†

[a]*School of Environmental Science and Engineering, Nanjing Tech University, Nanjing 210009, PR China. E-mail: qijiejin@njtech.edu.cn; htxu@njtech.edu.cn*

[b]*Jiangsu Collaborative Innovation Center of Atmospheric Environment and Equipment Technology (CICAEET), Jiangsu Key Laboratory of Atmospheric Environment Monitoring and Pollution Control, School of Environmental Science and Engineering, Nanjing University of Information Science & Technology, Nanjing 210044, PR China*

[c]*School of Chemistry and Chemical Engineering, Shandong University of Technology, Zibo, 255049, PR China*

2.1 Catalyst preparation

Firstly, 40 g of TiOSO$_4$ was dissolved in 200 g of distilled water, and stirred in a water bath at 90 °C. Then 3.208 g of ammonium metatungstate and an appropriate amount of citric acid monohydrate were dissolved in the TiOSO$_4$ solution. Next, 0.523 g of ZrOCl$_2$·8H$_2$O was dissolved in the mixed solution. After the mixed solution was stirred in a water bath at 90 °C to form the colorless, transparent and viscous colloid, it was dried at 110 °C. Finally, the samples were calcined at 600 °C for 2 h to obtain the catalysts. Among them, the loading amounts of WO$_3$ and ZrO$_2$ were 15 wt% and 1 wt%, respectively. The addition amount of citric acid monohydrate was 0 g, 5 g, 10 g and 15 g, respectively. Therefore, the catalysts were designated as WZ/T, 5C-WZ/T, 10C-WZT and 15C-WZ/T, respectively.

2.2 Catalysis measurement and characterization

2 mL of the sample was added into the fixed-bed quartz reactor (Fig. 1) to investigate the catalytic performance of NH$_3$-SCR. The reactant gas consisted of 500 ppm NO, 500 ppm NH$_3$, 200 ppm SO$_2$ (when used), 5 vol% H$_2$O (when used), 10 vol% O$_2$ and balance N$_2$. The total gas flow rate was 500 mL min^{-1} and the gas hourly space velocity (GHSV) were 15 000 h^{-1}. The flue gas analyzer (MRU VarioPlus, Germany) and the FTIR spectrometer (Gasmet FTIR DX4000) were used to measure the content of NO, NO$_2$, N$_2$O and NH$_3$. The NO$_x$ conversion and the N$_2$ selectivity were calculated by eqn (1) and (2).[24,25]

$$NO_x \text{ conversion} = \frac{[NO_x]_{in} - [NO_x]_{out}}{[NO_x]_{in}} \times 100\% \quad (1)$$

$$N_2 \text{ selectivity} = 1 - \frac{2[N_2O]_{out}}{[NO_x]_{in} + [NH_3]_{in} - [NO_x]_{out} - [NH_3]_{out}} \times 100\% \quad (2)$$

3. Results and discussion

3.1 Catalytic performance

Fig. 1 showed the catalytic efficiency and N$_2$ selectivity of different catalysts. As shown in Fig. 1(a), the NO conversion of

the WZ/T catalyst reached 63.8% at 350 °C, and was close to 100% at 450–550 °C. Correspondingly, the NO conversion at 300–400 °C was increased obviously when the citric acid monohydrate was added during the preparation process. The NO conversion of 5C-WZ/T at 350–550 °C was close to 100%, and the NO conversion at 300 °C was 56.9% higher than that of WZ/T (increased from 16.8% to 73.7%). In addition, the catalytic activity of 10C-WZ/T and 15C-WZ/T decreased when the amount of citric acid monohydrate continued to increase, but it was still higher than that of WZ/T. It was speculated that excessive citric acid monohydrate would cause the collapse of pores, and the presence of excessive reducing atmosphere would reduce the concentration of chemisorbed oxygen on the catalyst surface. Furthermore, the addition of citric acid monohydrate during the preparation process could also significantly reduce the bulk density of the catalyst. Although the amount of catalyst was 2 mL, the mass of 5C-WZ/T was only 57% of that of WZ/T. In other words, the appropriate amount of citric acid monohydrate could improve the catalytic performance at high weight hourly space velocity (WHSV). This would significantly reduce the cost of the catalyst, which was conducive to the practical application in engineering. Finally, as shown in Fig. 1(b), 5C-WZT had good N$_2$ selectivity, and its N$_2$ selectivity was higher than 90% at 300–600 °C. The by-product at low temperature was mainly NO$_2$, and it was mainly N$_2$O at high temperature.

In order to compare with the previous work (15W1ZT catalyst),[26] the 15W1ZT catalyst was tested under the same conditions, and the results were shown in Fig. S1.† Comparing 5C-WZ/T and 15W1ZT, it was seen that although the N2 selectivity of 5C-WZ/T at 250–350 °C was slightly lower than that of 15W1ZT, the NO$_x$ conversion was significantly higher than that of 15W1ZT in the temperature range of 250–600 °C. This proved the superiority of 5C-WZ/T catalyst with hierarchical pore structure in terms of SCR performance in another aspect.

Fig. 2 displayed the sulfur and water poisoning resistance of the 5C-WZ/T catalyst at 500 °C and 300 °C. As shown in Fig. 2(a), no matter how SO$_2$ and/or H$_2$O were introduced into the flue gas, the NO conversion of the 5C-WZ/T catalyst at 500 °C basically remained unchanged. This is because NH$_4$HSO$_4$ cannot be
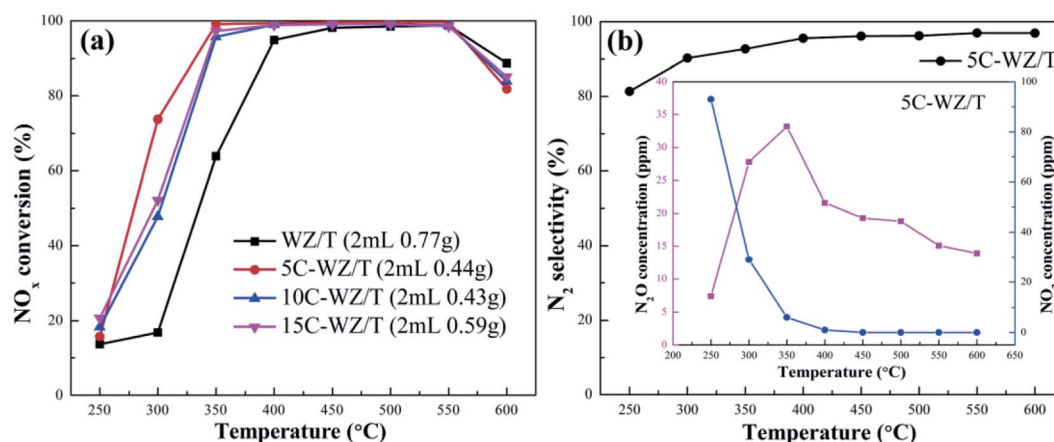

Fig. 1 (a) NO conversion of different catalysts; (b) N$_2$ selectivity of 5C-WZ/T catalyst. Reaction condition: 500 ppm NO, 500 ppm NH$_3$, 10% O$_2$, GSHV of 15 000 h^{-1} and N$_2$ balance gas.
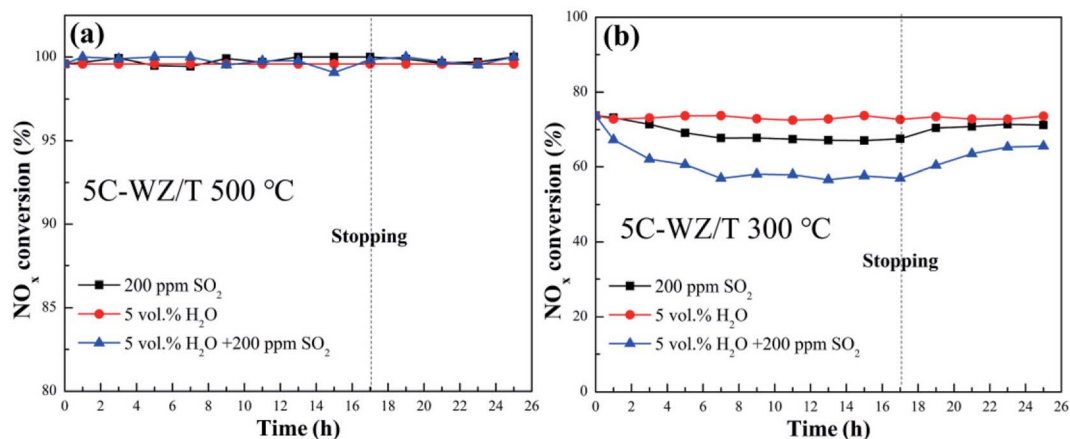
Fig. 4 FE-SEM images of different catalysts: (a) and (b) WZ/T; (c) and (d) 5C-WZ/T.

catalyst particles undergo secondary roasting, the catalytic activity was improved at low temperature. However, the NO conversion was still lower than that of 5C-WZ/T and other catalysts. This indicated that the hierarchical pore structure was indeed beneficial to the improvement of catalytic performance.
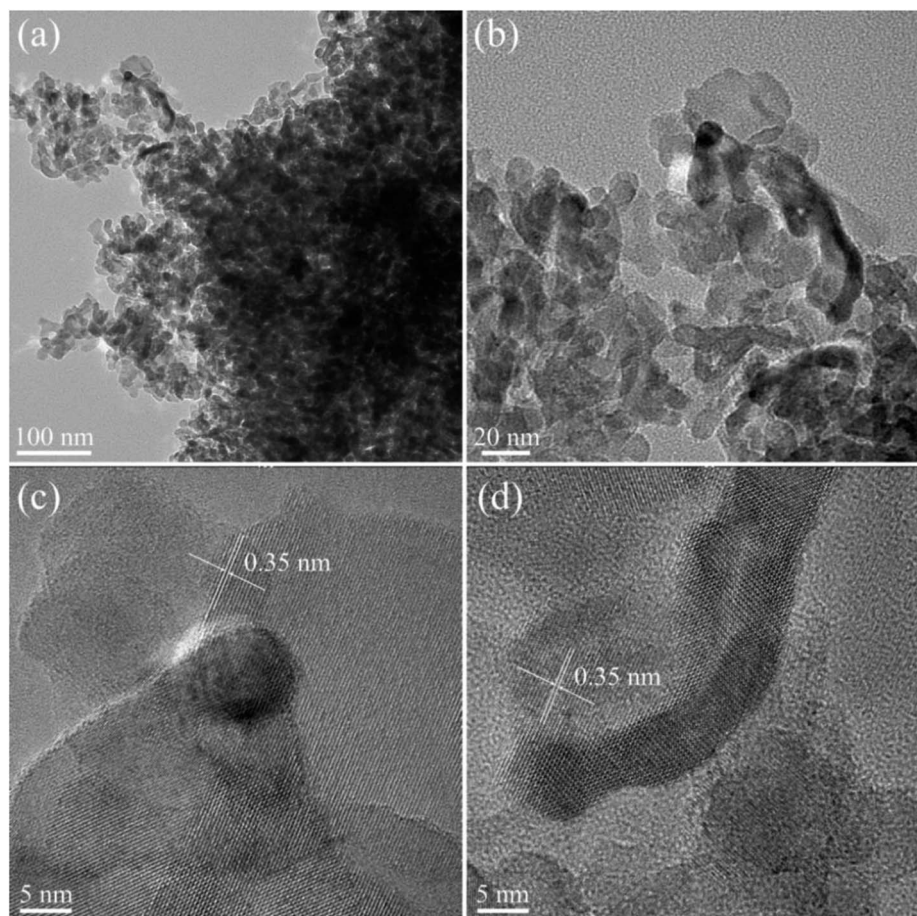
Fig. 5 TEM images of WZ/T catalyst.

Fig. 4 showed the FE-SEM pictures of WZ/T and 5C-WZ/T. As shown in Fig. 4(a) and (b), WZ/T was composed of rod-shaped particles with a diameter of 30 nm. Meanwhile, the rod-shaped particles were more evenly dispersed, but there were no obvious macropores. Correspondingly, with the addition of the appropriate amount of citric acid monohydrate, the 5C-WZ/T catalyst was also composed of spherical particles with a diameter of 30 nm and formed sub-micron pores. Combined with the following pore size distribution data (Fig. S4†), it indicated that the 5C-WZ/T catalyst had a hierarchical pore structure. This interpenetrating hierarchical pore structure was beneficial to exposing more active sites, and contributed to the adsorption and activation of reactant molecules, thereby improving the catalytic performance.

Fig. 5 showed the TEM picture of the WZ/T catalyst. From Fig. 5(a) and (b), it could be seen that the WZ/T catalyst was composed of rod-shaped nano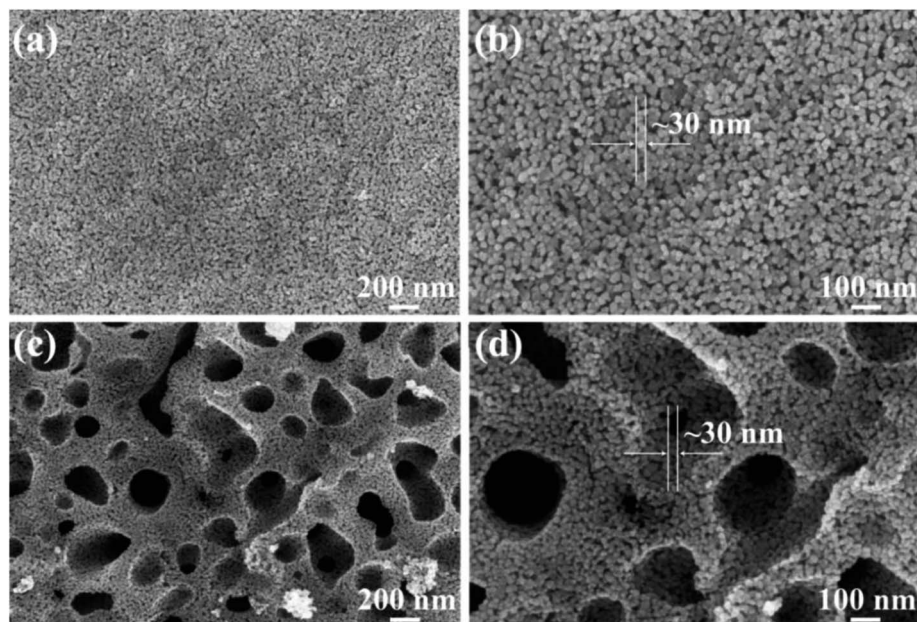particles, and the dispersion was relatively uniform. From Fig. 5(c) and (d), the lattice fringe with an interplanar spacing of 0.35 nm was consistent with the d-spacing of (101) facet of anatase TiO_2, respectively.[29,30]

Fig. 6 displayed the TEM picture of the 5C-WZ/T catalyst. From Fig. 6(a) and (b), it could be observed that the 5C-WZ/T catalyst was composed of uniformly dispersed spherical nanoparticles. Meanwhile, the interplanar spacing of the lattice fringe was also 0.35 nm. In addition, according to Fig. S3,† it was seen that the Ti, W, Zr and O elements were uniformly distributed. From Fig. 4, it could be observed that W–Zr-O_x/TiO_2 was a hierarchical pore structure formed by the agglomeration of uniform nanospheres. Therefore, it was indicated that WO_3 and ZrO_2 were not loaded on the surface of TiO_2 nanoparticles, but formed the spherical nanoparticles together with TiO_2.

Table 1 showed the specific surface area, pore volume and average pore diameter of different catalysts. The specific surface area of WZ/T was only 11.8 m^2 g^{-1}, and the average pore diameter was 14.9 nm. It proved from the side that the precursor of $TiOSO_4$ did not generate TiO_2 due to high temperature calcination. In addition, the specific surface areas of 5C-WZ/T, 10C-WZ/T and 15C-WZ/T were 89.8 m^2 g^{-1}, 117.2 m^2 g^{-1} and 106.4 m^2 g^{-1}, respectively. It showed that citric acid monohydrate played an important role in pore formation. Compared with the common $V_2O_5(WO_3)/TiO_2$ and $V_2O_5(MoO_3)$/
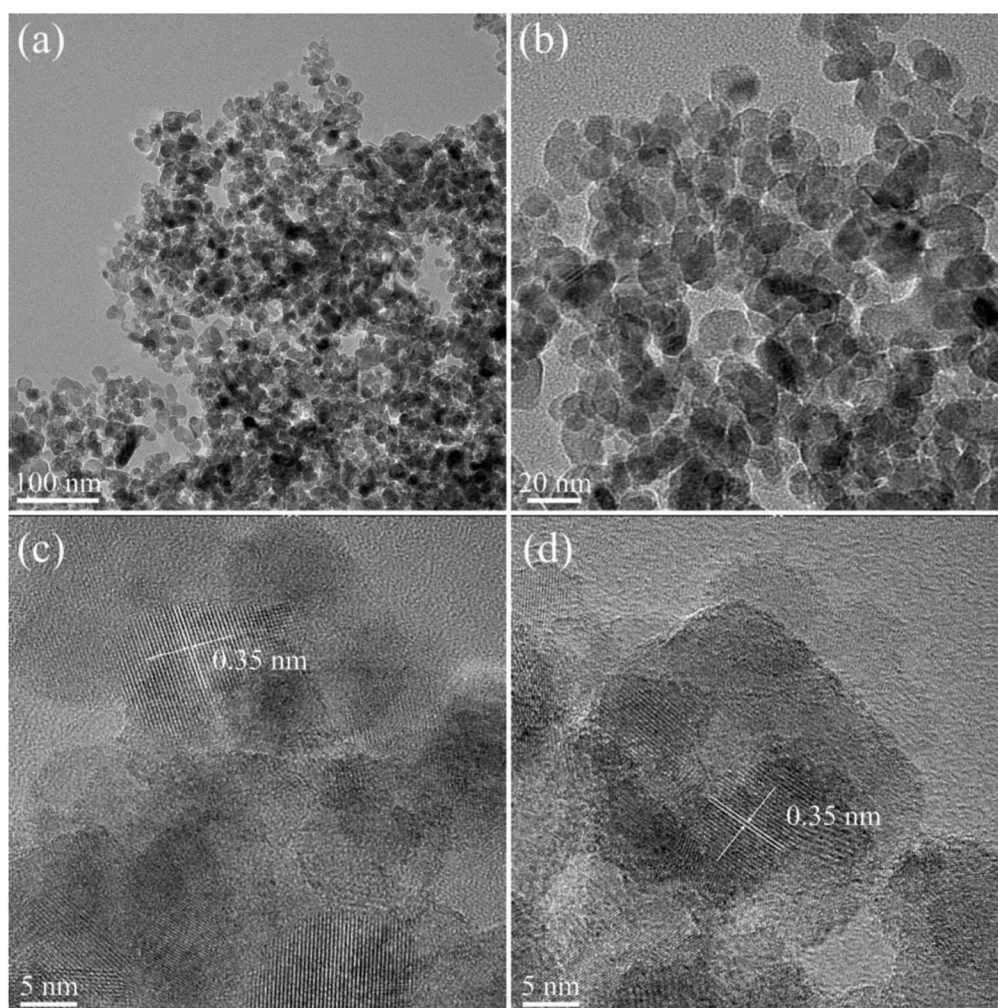

Fig. 6 TEM images of 5C-WZ/T catalyst.

Table 1 Physical properties of different catalysts

Samples	$S_{BET}/(m^2\ g^{-1})$	$V_{pore}/(cm^3\ g^{-1})$	D_{pore}/nm	Ref.
$V_2O_5(MoO_3)/TiO_2$	63.2	0.090	4.9	31
$V_{0.1}W_6Ti$	55.4	—	—	32
WZ/T	11.8	0.060	14.9	—
5C-WZ/T	89.8	0.481	18.3	—
10C-WZ/T	117.2	0.306	8.3	—
15C-WZ/T	106.4	0.267	7.4	—

TiO$_2$ catalysts in the literature,[31,32] the 5C-WZ/T, 10C-WZ/T and 15C-WZ/T catalysts had a larger specific surface area, which was conducive to the adsorption and activation of reactant molecules, and promote the improvement of catalytic performance. However, the average pore size gradually decreased with the increase of citric acid monohydrate. This meant that the excessive amount of citric acid monohydrate may cause some of the larger pores to collapse. It can also be seen from Fig. S4† that the most probable aperture was also gradually reduced. Finally, according to the results of FE-SEM and pore size distribution, it could be concluded that the 5C-WZ/T catalyst had a hierarchical pore structure.

The acidity affected the adsorption of NH$_3$ molecules, thereby determining the catalytic performance.[33–35] The NH$_3$-TPD results of WZ/T, 5C-WZ/T, 10C-WZ/T and 15C-WZ/T were shown in Fig. 7. The ammonia desorption peak was divided into three types: (1) the desorption peak at 50–200 °C was attributed to physical adsorption of ammonia; (2) the desorption peak at 200–400 °C corresponded to weak acidity; (3) the ammonia desorption peak at 400–550 °C corresponded to strong acidity.[36] For the four groups of catalysts, the temperature difference of the ammonia desorption peak was not obvious, indicating that the addition of citric acid monohydrate had little effect on the acid strength. As shown in Fig. 7(b), after the pores were made with citric acid monohydrate, the amount of strong acid obtained by the catalyst was reduced while the amount of weak acid was significantly increased. According to our previous

research, the strong acid of W–Zr-O$_x$/TiO$_2$ catalyst corresponded to Brønsted acid, and the weak acid corresponded to Lewis acid.[23] Therefore, it could be guessed that citric acid monohydrate provided a reducing atmosphere during the roasting process, which reduced the number of hydroxyl groups on the catalyst surface, thereby reducing the number of Brønsted acid. It was precisely because of the decrease in the amount of Brønsted acid that the NO conversion of the 5C-WZ/T, 10C-WZ/T and 15C-WZ/T catalysts at 600 °C was reduced. However, the increase in the amount of weak acid was conducive to the adsorption of ammonia molecules, thereby increasing the NO conversion of the catalyst at low temperatures. Finally, compared with the total acid quantity of V$_2$O$_5$-WO$_3$/TiO$_2$ (0.13 mmol g^{-1} and 0.20 mmol g^{-1}), W–Zr-O$_x$/TiO$_2$ had a higher acid quantity.[37,38] It was conducive to the adsorption and reaction of reactant molecules on the catalyst surface, thereby improving the catalytic activity at high temperature.

Fig. 8 displayed the H$_2$-TPR results of WZ/T, 5C-WZ/T, 10C-WZ/T and 15C-WZ/T to evaluate the redox performance. The broad peak at 400–700 °C should correspond to the reduction of Ti^{4+} to Ti^{3+}.[39,40] As shown in Fig. 8(a), although the WZ/T catalyst had the highest hydrogen consumption (3.21 mmol g^{-1}), the hydrogen reduction peak temperature was also the highest (640 °C). As the addition of citric acid monohydrate increased, the reduction peak temperature gradually decreased (from 537 °C to 514 °C). It indicated that the addition of citric acid monohydrate not only changed the microscopic morphology of the catalyst, but also enhanced the redox performance of the catalyst. It was mainly due to the reducing atmosphere formed during the roasting process of citric acid monohydrate, which gradually transformed Ti^{4+} to Ti^{3+} ions, and consumed the chemisorbed oxygen and hydroxyl on the catalyst surface. Therefore, the enhancement of redox properties at low temperature increased the NO conversion of the 5C-WZ/T catalyst.

3.3 Surface analysis

Fig. 9 and S5† showed the XPS high-resolution scan spectra of WZ/T, 5C-WZ/T, 10C-WZ/T and 15C-WZ/T catalysts. Table 2
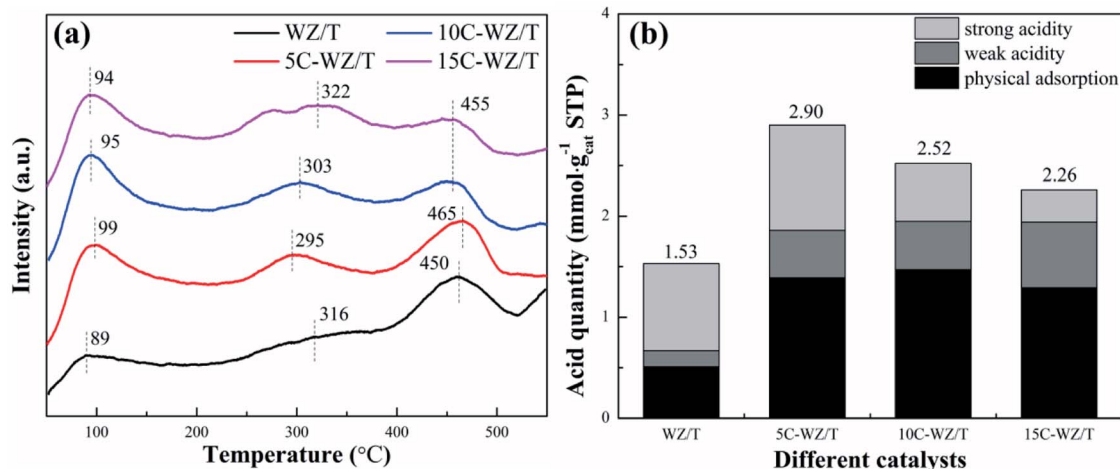
Fig. 7 (a) NH$_3$-TPD profiles and (b) acid quantity of different catalysts.
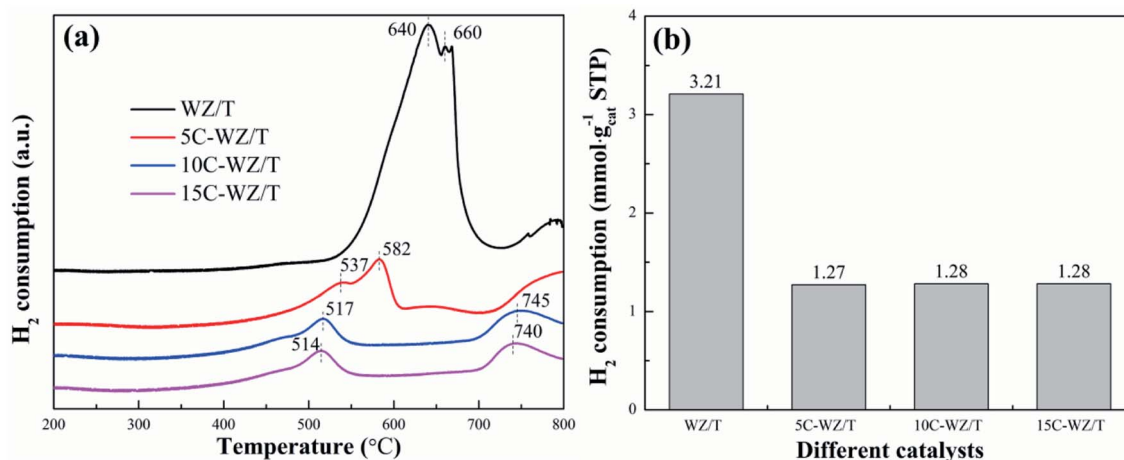
Fig. 8 (a) H_2-TPR profiles and (b) H_2 consumption of different catalysts.

calculated the atomic ratio of the catalyst surface. According to Fig. 9(a), the peaks of Ti 2p were divided into two types according to the electron binding energy: (1) the peaks at 464.6 eV and 458.5 eV were attributed to Ti^{4+}; (2) the peak at 463.4 eV corresponded to Ti^{3+}.[41] Compared with the spectral peaks of WZ/T catalysts, that of 5C-WZ/T, 10C-WZ/T and 15C-WZ/T catalysts shifted to the low electron binding energy, which was mainly because the reducing atmosphere changed the chemical environment of catalyst surface atoms. Meanwhile, the Ti^{3+} ion concentrations of WZ/T, 5C-WZ/T, 10C-WZ/T
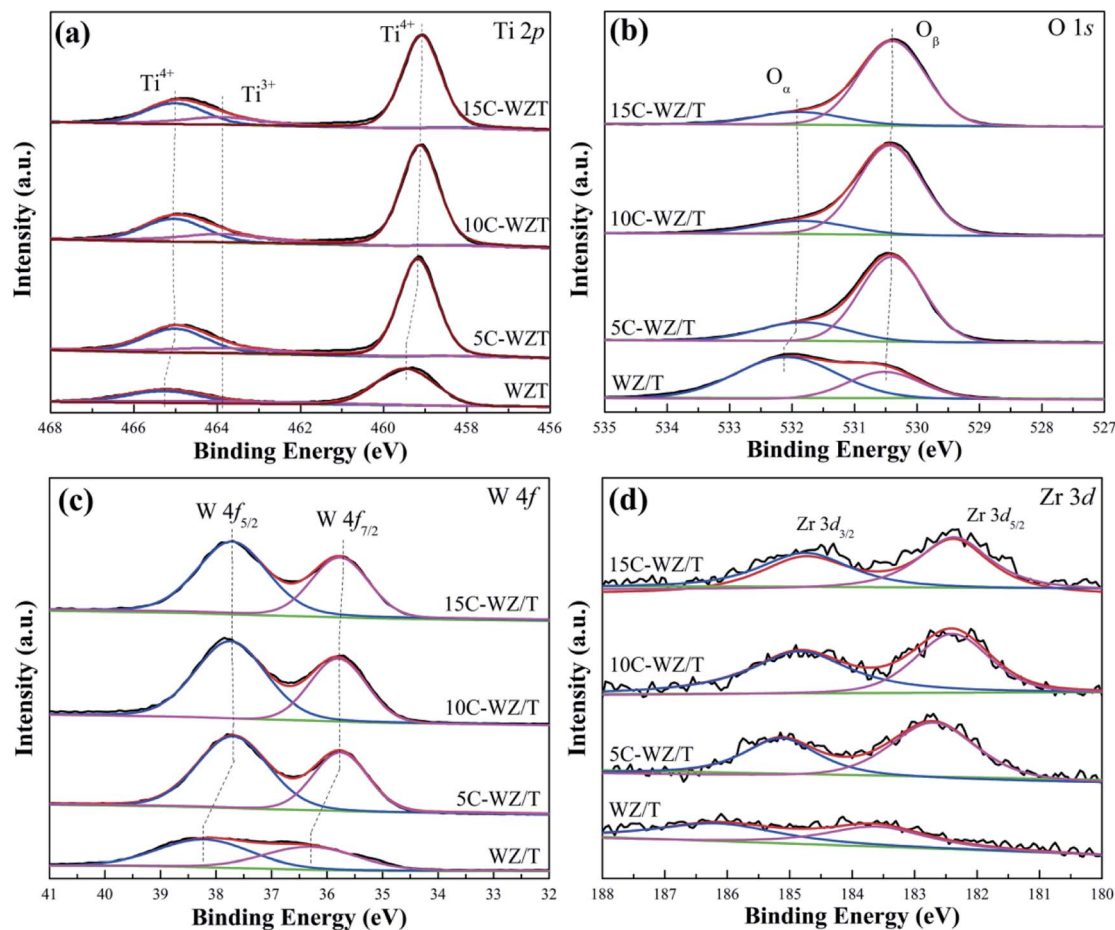
Fig. 9 (a) Ti 2p, (b) O 1s, (c) W 4f and (d) Zr 3d XPS high-resolution scans spectra of different catalysts.

Table 2 Atomic ratios on the surface of different catalysts

Sample	$Ti^{3+}/(Ti^{3+} + Ti^{4+})$	$O_\alpha/(O_\alpha + O_\beta)$
WZ/T	0.12	0.69
5C-WZ/T	0.14	0.23
10C-WZ/T	0.17	0.17
15C-WZ/T	0.18	0.16

and 15C-WZ/T gradually increased. It was mainly because the reducing atmosphere caused by citric acid monohydrate made Ti^{4+} transformed to Ti^{3+}. In other words, it also increased the oxygen vacancy concentration of the catalyst to a certain extent, thereby improving the catalytic performance.

From Fig. 9(b), the O 1s could be divided into chemisorbed oxygen (O_α, 531.2 eV) and lattice oxygen (O_β, 529.6 eV).[42–44] Similar to the change of the Ti 2p, the addition of citric acid monohydrate caused the shift of the O 1s. Compared with WZ/T, the chemisorbed oxygen concentrations of 5C-WZ/T, 10C-WZ/T and 15C-WZ/T decreased obviously. It was consistent with the H_2-TPR results, indicating that the addition of citric acid monohydrate reduced the hydrogen consumption and

chemisorbed oxygen concentration. The chemisorbed oxygen could participate in the reaction, thus promoting the reaction and improving the catalytic performance.[45,46] Therefore, the decrease of chemisorption oxygen concentration of 5C-WZ/T catalyst would lead to the decrease of catalytic activity. However, the hierarchical pore structure promoted the adsorption and activation of ammonia and other reactive molecules, thereby improving the catalytic performance.

Fig. 9(c) and (d) displayed the W 4f and Zr 3d XPS spectra of WZ/T, 5C-WZ/T, 10C-WZ/T and 15C-WZ/T catalysts. The peaks spanned at 34–36.5 eV (W $4f_{7/2}$) and 36.5–40 eV (W $4f_{5/2}$) corresponded to W^{6+} species.[47,48] Furthermore, the spectral peaks at 182 eV (Zr $3d_{5/2}$) and 185 eV (Zr $3d_{3/2}$) corresponded to Zr^{4+} species.[49]

3.4 Reaction mechanism

Fig. 10 displayed the *in situ* diffuse reflectance infrared spectrum of the 5C-WZ/T catalyst. Table 3 summarized the peaks and corresponding species. When NH_3 was adsorbed for 3 min, the coordinated NH_3 (3500–3100 cm^{-1} and 1601 cm^{-1}) and NH_4^+ (1468 cm^{-1}) appeared obviously on the catalyst surface. Meanwhile, the peak intensity of hydroxyl group (3646 and 1351 cm^{-1}) decreased gradually with the increase of time. This

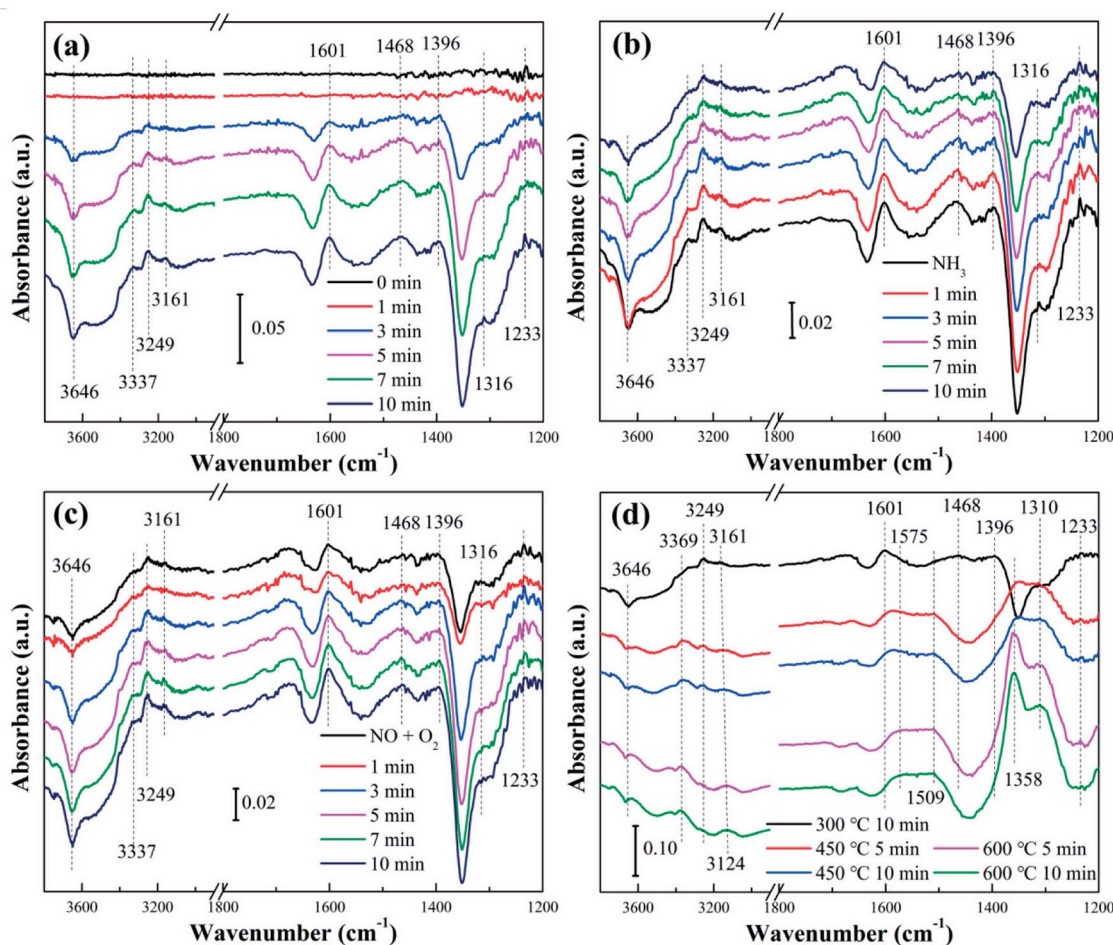**Fig. 10** *In situ* DRIFTS of 5C-WZ/T catalyst: (a) NH_3 adsorption at 300 °C, (b) NO + O_2 reacted with preadsorbed NH_3 at 300 °C, (c) NO + O_2 reacted with NH_3 at 300 °C, (d) NO + O_2 reacted with NH_3 at different temperatures.

Table 3 Details of the bands and corresponding species

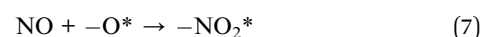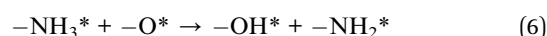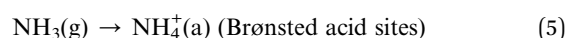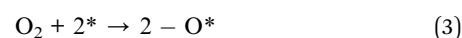| Band (cm^{-1})	Species	Ref.
3650–3640, 1351	Hydroxyl group	50
3500–3100	NH stretching vibration of coordinated NH$_3$	51
1601	NH bonds in coordinated NH$_3$ on Ti–O–Ti Lewis acid sites	39
1575	NH bonds in coordinated NH$_3$ on Lewis acid sites	52
1509	Bidentate nitrates	53
1468	The symmetric and asymmetric bending vibrations of NH$_4^+$	54
1400–1350	Monodentate nitrite	55
1316	Partially oxidized NH$_3$, such as N$_x$H$_y$O$_z$	56
1233	Bridging nitrates	39

indicated that both Lewis and Brønsted acids existed on the catalyst surface, and the main intermediate species of ammonia adsorbed on the catalyst surface were coordinated NH$_3$ and NH$_4^+$. Furthermore, the weak peaks of monodentate nitrite, partially oxidized NH$_3$ and bridging nitrates appeared. It indicated that the 5C-WZ/T catalyst had good redox performance (can also be verified in the H$_2$-TPR results). The appearance of monodentate nitrite species and bridging nitrates indicated that the hierarchical pore structure played an important role in the rapid conversion of reactive species on the catalyst surface. This conclusion could be confirmed in the H$_2$-TPR, NH$_3$-TPD and BET results. Compared with that of WZ/T, the hydrogen consumption concentration of 5C-WZ/T catalyst reduced. However, the addition of citric acid monohydrate enhanced the redox performance and promoted the increase of oxygen migration rate, which accelerated the transformation of reactant molecules.

As shown in Fig. 10(b), NO + O$_2$ was introduced and NH$_3$ was stopped when the catalyst adsorbed NH$_3$ for 10 min. The peaks of coordinated NH$_3$ on Lewis acid sites and NH$_4^+$ decreased with the increased of time. Meanwhile, the peak intensity of the monodentate nitrite (1396 cm^{-1}) and bridging nitrates (1233 cm^{-1}) also gradually decreased. Correspondingly, the peak intensity of partially oxidized NH$_3$ was slightly increased. It confirmed that coordinated NH$_3$, NH$_4^+$, monodentate nitrite and bridging nitrates were involved in the NH$_3$-SCR reaction. In other words, the NH$_3$-SCR reaction of the 5C-WZ/T catalyst at 300 °C followed the L-H mechanism.

After NO + O$_2$ was introduced for 10 min, NH$_3$ was added to make the SCR reaction continue to occur on the catalyst surface (Fig. 10(c)). It could be seen that there was no obvious change in all peaks. The main species on the catalyst surface were still coordinated NH$_3$ (3500–3100 cm^{-1} and 1601 cm^{-1}), NH$_4^+$ (1468 cm^{-1}) and monodentate nitrite (1396 cm^{-1}), and the peak intensity of other species was relatively weak. When the mixture of NH$_3$ + NO + O$_2$ was introduced and gradually heated (Fig. 10(d)), it could be observed that the spectral peaks of NH$_3$ intermediate species have gradually disappeared, while the spectral peaks of monodentate nitrite and bidentate nitrates gradually increased with the increase of time and reaction temperature (Fig. S6†). It indicated that the NH$_4^+$ was reacted with gas-phase NO$_2$. In other words, the NH$_3$-SCR reaction at the 450 °C followed E-R and L-H mechanisms simultaneously.

The NH$_3$-SCR reaction over 5C-WZ/T catalyst followed L-H mechanism at 300 °C and followed E-R and L-H mechanisms simultaneously at 450 °C. The *in situ* DRIFT spectra have proven

that the monodentate nitrite, bidentate nitrate, coordinated NH$_3$ and NH$_4^+$ existed over the 5C-WZ/T catalyst surface. Therefore, the reaction mechanism of 5C-WZ/T was proposed in eqn (3)–(11).

$$O_2 + 2* \rightarrow 2 - O* \tag{3}$$

$$NH_3 + * \rightarrow -NH_3* \tag{4}$$

$$NH_3(g) \rightarrow NH_4^+(a) \text{ (Brønsted acid sites)} \tag{5}$$

$$-NH_3* + -O* \rightarrow -OH* + -NH_2* \tag{6}$$

$$NO + -O* \rightarrow -NO_2* \tag{7}$$

$$NH_4^+(a) + -NO_2* \rightarrow NH_4NO_2 \rightarrow N_2 + 2H_2O \tag{8}$$

$$-NH_2* + -NO_2* \rightarrow N_2 + H_2O + -O* \tag{9}$$

$$2 - OH* \leftrightarrow H_2O + -O* \tag{10}$$

$$NH_4^+(a) + NO_2 \rightarrow NH_4^+NO_2 \rightarrow N_2 + H_2O \tag{11}$$
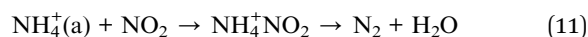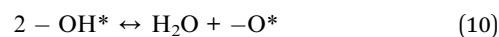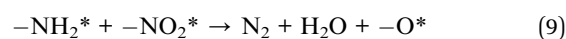
4. Conclusions

In this work, a series of W–Zr-O$_x$/TiO$_2$ catalysts with hierarchical pore structure were prepared, and used for the NH$_3$-SCR. The addition of citric acid monohydrate could make the catalyst form a hierarchical pore structure. It not only improved the specific surface area, redox performance, and acid quantity, but also enabled the catalyst to expose more active sites and improved the catalytic performance. Although the reducing atmosphere caused by citric acid monohydrate reduced the chemical adsorption oxygen concentration, it increased the oxygen mobility and Ti^{3+} ion concentration, which was more conducive to the improvement of catalytic activity. Finally, according to the *in situ* DRIFT spectra, the NH$_3$-SCR reaction over 5C-WZ/T catalyst followed L-H and E-R mechanisms. The monodentate nitrite, bidentate nitrate, gas-phase NO$_2$, coordinated NH$_3$ and NH$_4^+$ were the main reaction intermediate.

Conflicts of interest

There are no conflicts to declare.

Acknowledgements

Notes and references

1 D. H. Jo, G. T. Park, T. Ryu and S. B. Hong, *Appl. Catal., B*, 2019, **243**, 212–219.

2 A. Beretta, A. Lanza, L. Lietti, S. A. Clave, J. Collier and M. Nash, *Chem. Eng. J.*, 2019, **359**, 88–98.

3 S. Dahlin, C. Lantto, J. Englund, B. Westerberg, F. Regali, M. Skoglundh and L. J. Pettersson, *Catal. Today*, 2019, **320**, 72–83.

4 X. L. Hu, J. X. Chen, W. Y. Qu, R. Liu, D. R. Xu, Z. Ma and X. F. Tang, *Environ. Sci. Technol.*, 2021, **55**, 5435–5441.

5 S. H. Zhan, H. Zhang, Y. Zhang, Q. Shi, Y. Li and X. J. Li, *Appl. Catal., B*, 2017, **203**, 199–209.

6 Y. J. Pu, P. C. Wang, W. J. Jiang, Z. D. Dai, L. Yang, X. Jiang, Z. C. Jiang and L. Yao, *Chemosphere*, 2021, **284**, 131377.

7 Q. J. Jin, Y. S. Shen, Y. Cai, L. Chu and Y. W. Zeng, *J. Hazard. Mater.*, 2020, **381**, 120934.

8 X. L. Weng, X. X. Dai, Q. S. Zeng, Y. Liu and Z. B. Wu, *J. Colloid Interface Sci.*, 2016, **461**, 9–14.

9 T. Zhang, J. Liu, D. X. Wang, Z. Zhao, Y. C. Wei, K. Cheng, G. Y. Jiang and A. J. Duan, *Appl. Catal., B*, 2014, **148**, 520–531.

10 D. Wang, Q. Z. Chen, X. Zhang, C. Gao, B. Wang, X. Huang, Y. Peng, J. H. Li, C. M. Lu and J. Crittenden, *Environ. Sci. Technol.*, 2021, **55**, 2743–2766.

11 C. J. Tang, H. L. Zhang and L. Dong, *Catal. Sci. Technol.*, 2016, **6**, 1248–1264.

12 P. Xu, J. Zheng, F. L. Jing and W. Chu, *Mol. Catal.*, 2021, **508**, 111586.

13 J. L. Chen, G. Peng, W. Zheng, W. B. Zhang, L. Guo and X. Q. Wu, *Catal. Sci. Technol.*, 2020, **10**, 6583–6598.

14 E. Borfecchia, P. Beato, S. Svelle, U. Olsbye, C. Lamberti and S. Bordiga, *Chem. Soc. Rev.*, 2018, **47**, 8097–8133.

15 G. Li, B. D. Wang, Z. C. Wang, Z. H. Li, Q. Sun, W. Q. Xu and Y. L. Li, *J. Phys. Chem. C*, 2018, **122**, 20210–20231.

16 P. Wu, K. Shen, Y. L. Liu, Y. P. Zhang, G. B. Li, H. Q. Yang and S. Wang, *Catal. Sci. Technol.*, 2021, **11**, 4115–4132.

17 Y. X. Chen, Z. C. X. Dong, Z. W. Huang, M. J. Zhou, J. Y. Gao, J. X. Chen, C. Li, Z. Ma, J. M. Chen and X. F. Tang, *Catal. Sci. Technol.*, 2017, **7**, 2467–2473.

18 Z. H. Lian, S. H. Xin, N. Zhu, Q. Wang, J. Xu, Y. Zhang, W. P. Shan and H. He, *Catal. Sci. Technol.*, 2020, **10**, 311–314.

19 X. B. Wang, Q. Y. Fang, J. Wang, K. T. Gui and H. R. Thomas, *RSC Adv.*, 2020, **10**, 44876–44883.

20 P. Granger and V. I. Parvulescu, *Chem. Rev.*, 2011, **111**, 3155–3207.

21 J. X. Liu, H. F. Cheng, J. B. Tan, B. Liu, Z. H. Zhang, H. D. Xu, M. J. Zhao, W. S. Zhu, J. Liu and Z. Zhao, *J. Mater. Chem. A*, 2020, **8**, 6717–6731.

22 J. C. Chai, S. H. Zhu, Y. L. Cen, J. Guo, J. G. Wang and W. B. Fan, *RSC Adv.*, 2017, **7**, 8567–8574.

23 M. M. Chen, Q. J. Jin, X. J. Tao, Y. C. Pan and Y. S. Shen, *Catal. Today*, 2020, **358**, 254–262.

24 Y. K. Yu, X. F. Yi, J. L. Zhang, Z. J. Tong, C. W. Chen, M. D. Ma, C. He, J. X. Wang, J. S. Chen and B. B. Chen, *Catal. Sci. Technol.*, 2021, **11**, 5125–5134.

25 Y. K. Yu, J. L. Zhang, C. W. Chen, M. D. Ma, C. He, J. F. Miao, H. R. Li and J. S. Chen, *New J. Chem.*, 2020, **44**, 13598–13605.

26 Q. J. Jin, Z. W. Xue, X. H. Zhi, W. Y. Ji, Y. S. Shen and Y. W. Zeng, *Fuel*, 2021, **305**, 121534.

27 J. Y. Lu, Z. Y. Zhou, H. Z. Zhang and Z. Yang, *Fuel*, 2019, **245**, 528–533.

28 G. Y. Zhou, P. Maitarad, P. L. Wang, L. P. Han, T. T. Yan, H. R. Li, J. P. Zhang, L. Y. Shi and D. S. Zhang, *Environ. Sci. Technol.*, 2020, **54**, 13314–13321.

29 Q. J. Jin, Y. S. Shen and S. M. Zhu, *J. Colloid Interface Sci.*, 2017, **487**, 401–409.

30 W. Wang, C. H. Lu, Y. R. Ni, F. P. Peng and Z. Z. Xu, *Appl. Surf. Sci.*, 2013, **265**, 438–442.

31 B. Zhao, X. W. Liu, Z. J. Zhou, H. Z. Shao, C. Wang and M. H. Xu, *Fuel Process. Technol.*, 2015, **134**, 198–204.

32 L. Chen, J. H. Li and M. F. Ge, *J. Phys. Chem. C*, 2009, **113**, 21177–21184.

33 L. Lietti, I. Nova, E. Tronconi and P. Forzatti, *Catal. Today*, 1998, **45**, 85–92.

34 W. Y. Qu, X. N. Liu, J. X. Chen, Y. Y. Dong, X. F. Tang and Y. X. Chen, *Nat. Commun.*, 2020, **11**, 1532.

35 J. J. Liu, G. Z. He, W. P. Shan, Y. B. Yu, Y. L. Huo, Y. Zhang, M. Wang, R. Yu, S. S. Liu and H. He, *Appl. Catal., B*, 2021, **291**, 120125.

36 P. Ning, Z. X. Song, H. Li, Q. L. Zhang, X. Liu, J. H. Zhang, X. S. Tang and Z. Z. Huang, *Appl. Surf. Sci.*, 2015, **332**, 130–137.

37 Z. Liu, J. Han, L. Zhao, Y. W. Wu, H. X. Wang, X. Q. Pei, M. X. Xu, Q. Lu and Y. P. Yang, *Appl. Catal., A*, 2019, **587**, 117263.

38 X. Xiao, S. C. Xiong, B. Li, Y. Geng and S. J. Yang, *Catal. Lett.*, 2016, **146**, 2242–2251.

39 Q. J. Jin, Y. S. Shen, L. Ma, Y. C. Pan, S. M. Zhu, J. Zhang, W. Zhou, X. F. Wei and X. J. Li, *Catal. Today*, 2019, **327**, 279–287.

40 W. Y. Jiang, Y. L. Yu, F. Bi, P. F. Sun, X. L. Weng and Z. B. Wu, *Environ. Sci. Technol.*, 2019, **53**, 12657–12667.

41 K. J. Duan, Z. H. Wang, C. Hardacre, Z. M. Liu, S. Chansai and C. Stere, *Catal. Today*, 2019, **332**, 69–75.

42 K. Lee, B. Choi, C. Lee and K. Oh, *J. Ind. Eng. Chem.*, 2020, **90**, 132–144.

43 Q. J. Jin, M. M. Chen, X. J. Tao, B. X. Lu, J. Y. Shen, Y. S. Shen and Y. W. Zeng, *Appl. Surf. Sci.*, 2020, **512**, 145757.

44 S. H. Zhang, Y. Y. Li, J. H. Huang, J. Lee, D. H. Kim, A. I. Frenkel and T. Kim, *J. Phys. Chem. C*, 2019, **123**, 7166–7177.

45 Y. K. Yu, J. F. Miao, J. X. Wang, C. He and J. S. Chen, *Catal. Sci. Technol.*, 2017, **7**, 1590–1601.

46 L. Zhu, L. Zhang, H. X. Qu and Q. Zhong, *J. Mol. Catal. A: Chem.*, 2015, **409**, 207–215.

47 R. Camposeco, S. Castillo, V. Mugica, I. Mejía-Centeno and J. Marín, *Chem. Eng. J.*, 2014, **242**, 313–320.

48 X. M. Wang, X. S. Du, L. Zhang, Y. R. Chen, G. P. Yang and J. Y. Ran, *Appl. Catal., A*, 2018, **559**, 112–121.

49 J. H. Lin, C. P. Ma, Q. Wang, Y. F. Xu, G. Y. Ma, J. Wang, H. T. Wang, C. L. Dong, C. H. Zhang and M. Y. Ding, *Appl. Catal., B*, 2019, **243**, 262–272.

50 M. L. Ang, J. T. Miller, Y. Cui, L. Mo and S. Kawi, *Catal. Sci. Technol.*, 2016, **6**, 3394–3409.

51 Y. Liu, W. L. Cen, Z. B. Wu, X. L. Weng and H. Q. Wang, *J. Phys. Chem. C*, 2012, **116**, 22930–22937.

52 F. Cao, J. Xiang, S. Su, P. Y. Wang, S. Hu and L. S. Sun, *Fuel Process. Technol.*, 2015, **135**, 66–72.

53 Z. M. Liu, Y. Yi, J. H. Li, S. I. Woo, B. Y. Wang, X. Z. Cao and Z. X. Li, *Chem. Commun.*, 2013, **49**, 7726–7728.

54 Y. J. Pan, B. X. Shen, L. J. Liu, Y. Yao, H. P. Gao, C. Liang and H. J. Xu, *Fuel*, 2020, **282**, 118834.

55 L. Chen, X. J. Yao, J. Cao, F. M. Yang, C. J. Tang and L. Dong, *Appl. Surf. Sci.*, 2019, **476**, 283–292.

56 L. Chen, J. H. Li and M. F. Ge, *Environ. Sci. Technol.*, 2010, **44**, 9590–9596.